

Background-oriented schlieren of entropy waves advected in straight duct

Markus WEILENMANN⁽¹⁾, Yuan XIONG⁽¹⁾, Nicolas NOIRAY⁽¹⁾

⁽¹⁾CAPS Laboratory, Mechanical and Process Engineering Department, ETH Zürich, Switzerland, noirayn@ethz.ch

Abstract

Entropy waves generate indirect combustion noise when accelerated in the turbine stages of aeroengines. This indirect combustion noise constitutes a significant part of the overall combustion noise. In addition, the indirect combustion noise from entropy waves can constructively interact with flame and induce high amplitude self-sustained oscillations. A deep understanding of the advection and dispersion of entropy waves is therefore important for the prediction of noise emissions and thermoacoustic instabilities. This experimental study contributes to that goal: a highly turbulent airflow in a rectangular duct at ambient temperature is subject to the forcing of a siren supplied with hot air. This pulsed hot-jet-in-cold-crossflow yields coherent entropy waves, which are advected through the channel. The line-of-sight integrated temperature amplitude and phase are measured using high-speed Background-oriented Schlieren (BOS), thermocouples and simultaneous particle image velocimetry (PIV). This non-invasive method facilitates the observation of low amplitude temperature fluctuations at high frequencies, with a simple and inexpensive setup.

Keywords: Sound, Entropy waves

1 INTRODUCTION

Combustion systems in general, but gas turbines and aero-engines in particular, are prone to combustion noise that comprises two components: direct combustion noise and indirect combustion noise. The direct component originates from the unsteady volume expansion caused by fluctuating heat release of non steady flames [1, 11, 2], that are present in all gas turbine applications. The unsteady heat release also modulates the temperature of the exhaust gas stream and therefore creates hot pockets which are advected downstream with the flow. These travelling temperature waves are generally referred to as Entropy Waves [7]. When they are accelerated in a nozzle, or for example a turbine inlet, indirect noise is generated [6]. To correctly predict indirect noise, it is of great importance to understand and quantify the dispersion of entropy waves during their advection in the combustion chamber. Recently, significant effort was put into the modeling of such decay processes [5, 8]. The goal of this work is to measure such entropy waves during the advection process.

2 EXPERIMENTAL SETUP

2.1 Test rig specifications

The ETH high-speed test rig is a non-reactive air wind tunnel with rectangular cross-section depicted in figure 1. A compressor is supplying dry air at a maximal mass flow of 240 g/s at 5.5 bar. For this study, the test rig was operated at a static pressure of around 1.3 bar. The channel has an inner height of $H = 57\text{mm}$ and a width of $W = 25\text{mm}$. Optical access is available in the test section from the top and the side using borosilicate windows.

Entropy waves are generated by a siren upstream of the test section. The siren consist of a rotating perforated disk and an electric heater, as schematically drawn in figure 2. The modulation frequency of this pulsed hot jet-in-crossflow is controlled by adjusting the rotational velocity of the disk. The temperature is controlled by thermostat, monitoring the temperature downstream of the heating element. The generated entropy waves are then advected to the test section where the optical measurements are performed. The walls of the siren are isolated while the main channel is exposed to natural convection of the surrounding air at room temperature.

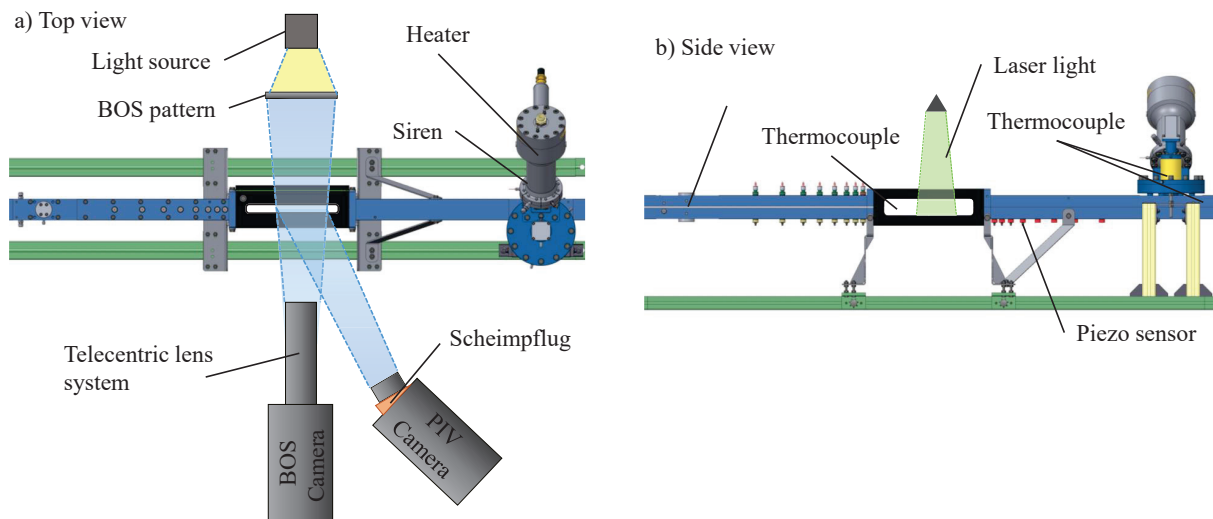


Figure 1. Experimental setup

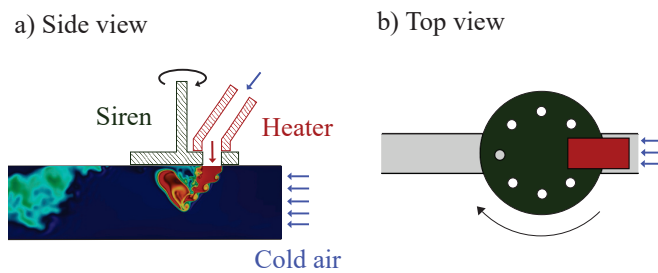


Figure 2. Siren operating principle

2.2 Instrumentation

To obtain the desired high-speed temperature measurements, a background oriented schlieren (BOS) system with telecentric optics was mounted perpendicular to the flow direction, as shown in figure 1 a). To avoid the strong mechanical vibrations induced by the siren, the BOS camera (Photron HSSX) plus optics (2 simple plano-convex lenses, Thorlabs LA1979 and Eksma 110-0730E), background pattern and light source (HARDsoft IL-106) were attached to one single optical rail that was isolated using passive pneumatic vibration dampers (Thorlabs PWA074). A second high-speed camera to do PIV was placed on a tripod in the same horizontal plane as the BOS system. The field of view (FOV) was adjusted to match the BOS one and the tilted focal plane was corrected using a Scheimpflug. The PIV camera was equipped with a Nikon AF 200mm micro Nikkor lens and a 532nm bandpass filter from Edmund Optics. A Photonics DM60 Nd:YAG was used to generate a pulsed 532 nm laser light sheet that was introduced in the center of the channel from the top using a laser arm and sheet optics from Lavisision.

To capture the mean temperatures of the main flow, the heated siren flow and the vitiated flow, thermocouples were placed at the three locations specified in figure 1 b). Additionally, a differential static pressure probe was placed downstream of the test section and the current ambient air pressure was noted during the experiments.

3 EXPERIMENTAL METHODOLOGY

3.1 Telecentric BOS

Telecentric BOS relies on the same principles as conventional BOS [10], which is the bending of light rays in non-homogeneous media due to spatial gradients in refractive index, but brings the advantage of increased depth of field and parallel projection of the background through the observation area and therefore also higher accuracy [9]. The setup consist of a high-speed camera, 2 convex lenses with focal lengths f_1 and f_2 , an aperture, a luminous light source and pattern of randomly placed dots. Such a setup is schematically drawn in figure 3, where Z_d is the distance between the background plane and the center of the observation area, Z_a the distance between the center of the observation area and Lens 1. The aperture is placed in between Lens 1 and Lens 2 where the distances between the lenses and the aperture are determined by the lenses focal lengths f_1 and f_2 . This allows to block most of the non-parallel light [9] and therefore increases the depth of field and ensures parallel projection of the background pattern through the observation area. With smaller aperture, depth of field increases, but the light intensity on the camera sensor decreases. Only a small fraction of the light is parallel or close to parallel, therefore a strong light source is needed along with a compromise on depth of field. This is quantified in more detail below.

Without being deflected by an inhomogeneous media in the observation area, a light ray may travel from the background pattern to the camera sensor via the path depicted by a dashed line in figure 3. If gradients in refractive index are present, the light ray is deflected by an angle ε . BOS is a line-of-sight integrated method, which means that ε can only be related to line-of-sight integrated gradients in refractive index n as shown in equation 1 [12], where s and q are the local coordinates tangential and perpendicular to the light ray and n_0 is the refractive index at room temperature.

$$\varepsilon = \frac{1}{n_0} \int \frac{dn}{dq} ds \quad (1)$$

Assuming a two-dimensional flow and small deflection angles, the deflection angle in y direction ε_y can be expressed as shown below with W being the thickness of the flow.

$$\varepsilon_y = \frac{W}{n_0} \frac{\partial n}{\partial y} \quad (2)$$

Since we are assuming small deflection angles, we can also relate the deflection angle to the apparent displacement Δ_y of the background pattern using equation 3.

$$\varepsilon_y = \tan\left(\frac{\Delta_y}{Z_d}\right) \approx \frac{\Delta_y}{Z_d} \quad (3)$$

Combining equations 2 and 3 and considering deflection in x direction analogously, expressions for the first spatial gradients of refractive index as a function of the apparent pattern displacement are obtained:

$$\begin{aligned} \frac{\partial n}{\partial x} &= \frac{n_0}{W} \frac{\Delta_x}{Z_d} \\ \frac{\partial n}{\partial y} &= \frac{n_0}{W} \frac{\Delta_y}{Z_d} \end{aligned} \quad (4)$$

Since we can assume parallel projection in this telecentric optical system, the scaling between background and image sensor plane is defined only by the focal lengths f_1 and f_2 of the two lenses [9]. 3.

$$\frac{f_2}{f_1} = \frac{\Delta_y}{\Delta'_y} = M_{tele} \quad (5)$$

Practically, correct scaling is ensured using a calibration target on the background plane and the displacement Δ_y is obtained directly using the cross-correlation algorithm of Lavision DAVIS 8.4. Classically, the BOS methods

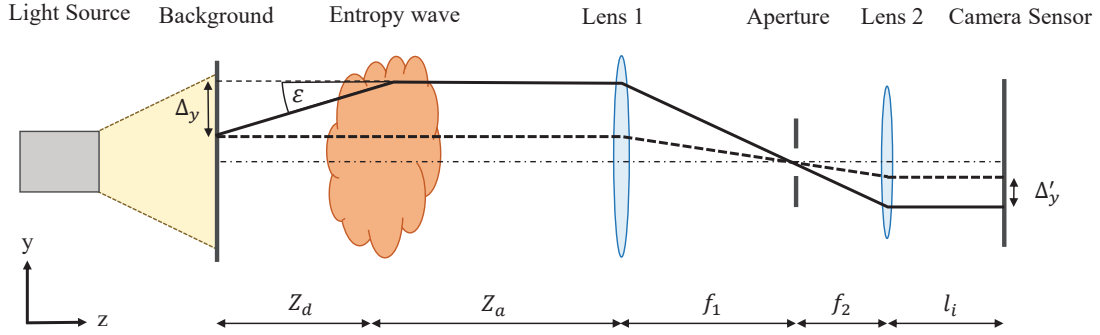


Figure 3. Telecentric BOS principle

requires a reference image of the background taken with clean optical path, meaning a homogenous medium in the observation area and therefore $\epsilon = 0$. This reference is then compared to snapshots later in time using cross-correlation when the optical path is affected by refractive index gradients. In highly vibrating environments and thermally unsteady experiments this can be a problem because high bias errors arise [13]. Even in a less harsh experimental environment, so called spurious displacements [14] can cause significant errors in the displacement quantification. Overall it is best to minimize the time between the recording of the reference image and the actual measurement. In this work, only moving fast moving gradient structures are considered, therefore a different strategy is employed. For each measurement, data sets of 5000 images were recorded at a frame-rate of 12.5 kHz and an average image was calculated to serve as reference. The slight blurriness resulting from this strategy was handled well by the cross-correlation algorithm.

The δ_x and δ_y fields were calculated employing a multi-pass strategy with decreasing correlation window size of 48 by 48 pixel with 75% overlap in the first pass and 16 by 16 pixel with 50% overlap in the second pass. Despite the very luminous LED light source (Model IL-106, HARDsoft Inc.), there is a trade-off between gathering enough light and improved depth of field due to a small aperture. An aperture diameter of $d = 4$ mm was found to allow for sufficient illumination even at this high frame-rate.

3.2 Processing

The telecentric BOS system described in section 3.1 yields instantaneous displacement fields Δ_x and Δ_y of the camera FOV. Using the velocity information obtained by PIV, these fields are spatially connected since the frame-rate is sufficiently high to have overlapping areas within the individual snapshots. Figure 4 a) shows such snapshots of the the total displacement $\Delta_{xy} = \sqrt{\Delta_x^2 + \Delta_y^2}$. Visually it is already obvious that there is significant overlap between the individual frames since the gradient structure that is advected through the FOV has an almost identical shape in all the displayed snapshots. The overlap $d(\phi)$ is estimated using a phase-averaged spatial average of the axial velocity at this instant. In the next step the overlapping areas are continuously averaged, as displayed in figure 4 b). Since the axial velocity is not constant over the acoustic cycle, the overlap d varies as well. This process is repeated over all available acoustic cycles to get the displacement field depicted in figure 4 c). Since the overlap is not constant, but the phase angle increases linearly with time, new coordinates \tilde{x} and \tilde{y} are needed:

$$\begin{aligned} \tilde{x} &= x_s + \frac{T_0}{2\pi} \int_0^\phi \tilde{u}(\phi) d\phi \\ \tilde{y} &= y_s \end{aligned} \quad (6)$$

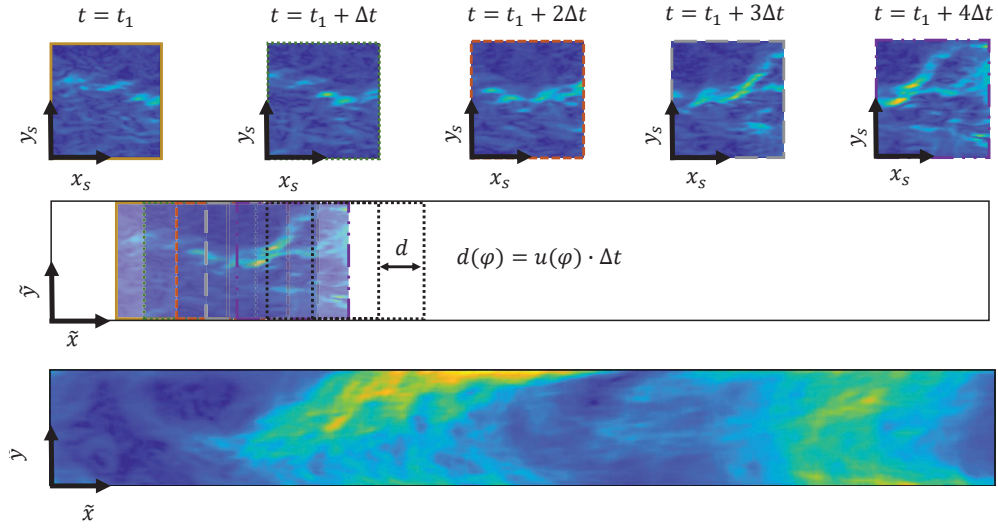


Figure 4. a) Instantaneous displacement fields of camera FOV b) Using the velocimetry data obtained by PIV, an overlap is calculated and the displacement fields are stacked on top of each other accordingly. In the overlapping area, the displacement fields are averaged. c) Resulting phase-averaged displacement field representing one acoustic cycle (here 240 Hz)

The displacement fields obtained by applying this method represent the phase-averaged mean of an entire convective wavelength, but captured sequentially at the camera position since the FOV is not wide enough to capture an instantaneous convective wave in one shot.

The same approach may also be used with instantaneous velocity data to get several instantaneous cycles. The axial coordinate would in that case change to:

$$\tilde{x}_{inst} = x_s + \int_0^t u(t) dt \quad (7)$$

To further process the obtained gradient fields, one needs to perform 2D spatial integration. This can be achieved by solving the system shown in equation 4. In this study the integration was done by taking the partial derivative in x and y respectively and adding the 2 equations which results in equation 8

$$\frac{\partial^2 n}{\partial x^2} + \frac{\partial^2 n}{\partial y^2} = \frac{n_0}{WZ_d} \left(\frac{\partial \Delta x}{\partial x} + \frac{\partial \Delta y}{\partial y} \right) \quad (8)$$

The two dimensional line-of-sight integrated refraction index field can then be obtained using a poisson solver. [14] The line-of-sight integrated density is obtained via the Gladstone-Dale equation shown below with G being the Gladstone-Dale constant [3].

$$\rho = \frac{n-1}{G} \quad (9)$$

Using the ideal gas law, one can then calculate the line-of-sight integrated temperature field, using the gas constant of air R and the static pressure p_s .

$$T = \frac{p_s}{\rho R} \quad (10)$$

4 RESULTS

4.1 Temperature and Mie scattering fields

Experiments were conducted at various excitation temperatures and frequencies. The mass flow rate of the cold main flow was kept at 150 g/s, while the overall mass flow of the oscillating hot jet-in-crossflow was kept at 10 % of the main flow. The temperature of the hot jet-in-crossflow was varied from 321K to 519K while the cold main flow was kept at 300K. Figure 5 shows the obtained line-of-sight integrated temperature fields for two siren frequencies and five amplitudes each. The increase in excitation temperature is easily visible, which is a good indication that the presented results are physical and entropy waves survive the advection process from siren injection to the test section. This also means that these waves would be relevant for indirect noise production, if an area change would be added to the channel. To support the claim of having measured the entropy waves correctly, the same processing algorithm

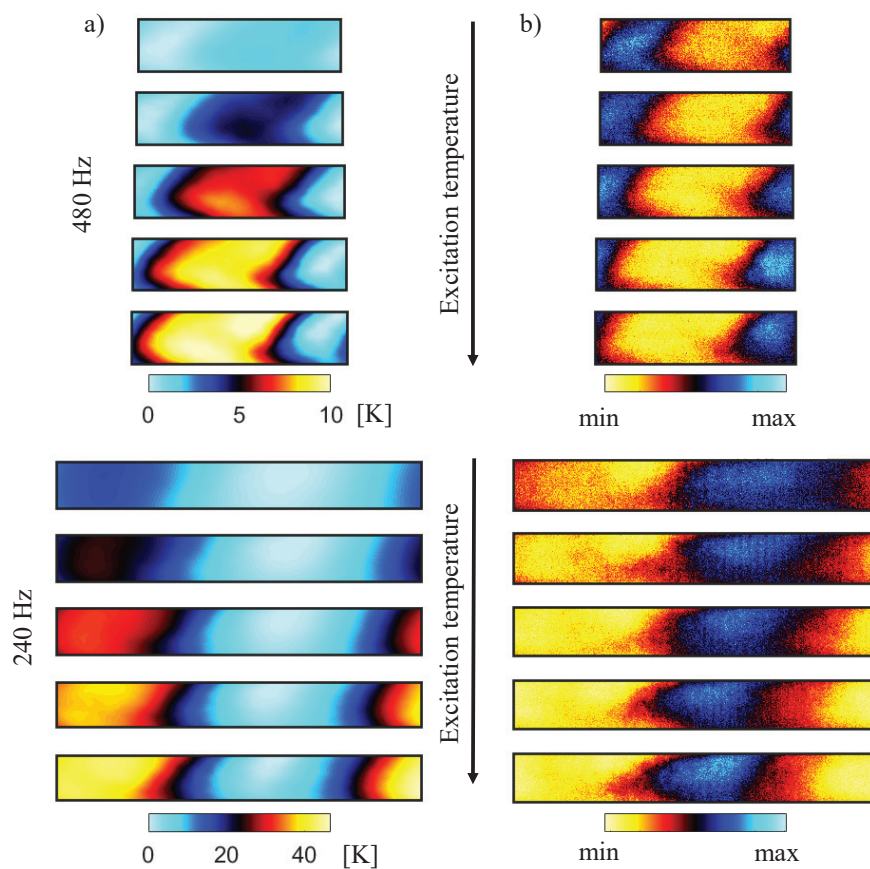


Figure 5. a) Phase-averaged amplitude fields of the fluctuating temperature component for increasing siren amplitudes and two frequencies b) Phase-averaged Mie scattering images

detailed in section 3.2 was applied to the Mie scattering images of the seeded flow, recorded to perform PIV. Since only the cold main flow was subject to particle seeding, one can qualitatively identify hot regions by looking at the intensity of this Mie scattering signal. Low luminosity corresponds therefore to a hot region and higher higher luminosity to a colder region where less or no mixing with the hot air, injected by the siren, has happened. The results presented in figure 5 b) are in good agreement with the BOS results.

4.2 Validation against LES

To validate the measured temperature amplitudes, large-eddy simulations (LES) were performed using the explicit parallel code AVBP [4], employing the second order numerical scheme Lax-Wendroff. Five simulations with similar conditions for mass flows, temperatures and pressure were performed in a domain representative of the experimental facilities. The intention was not to achieve a perfect match, but to show that the obtained BOS results are reasonable.

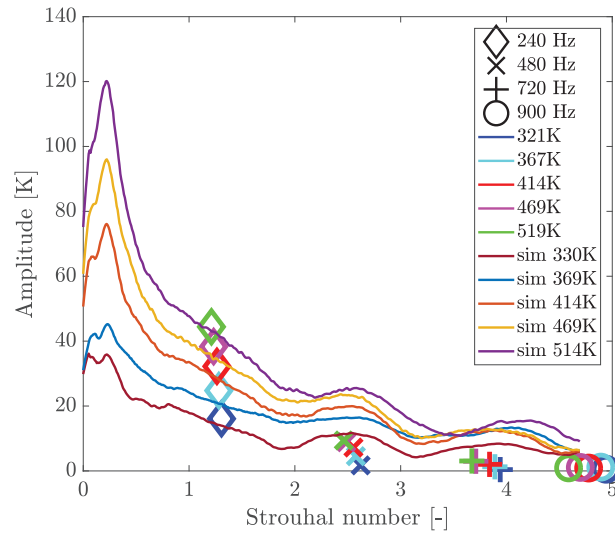


Figure 6. Phase-locked amplitudes of temperature obtained by experiments and LES as a function of Strouhal number

Figure 6 shows phase-locked amplitudes of the line-of-sight integrated temperature, extracted from the LES, as a function of the Strouhal number $Str = \frac{fL}{\bar{u}_c}$. L represents the axial distance from the siren injection hole, f the excitation frequency and \bar{u}_c the average advection velocity present in the channel. The agreement for low Str is quite good, but at higher Str , the LES consequently predicts a higher temperature fluctuation amplitude. This experimental method relies on spatial integration, which increases the difficulty to get a clean measurement when spatial separation of the entropy waves becomes smaller. This is the case for high Str numbers, especially since these points were measured using a higher excitation frequency, rather than increased distance. A large variation of L is difficult to achieve with this experimental facility, because the optical access is limited to the test section.

This issue and also the shape of the amplitude decay in the LES will be discussed in depth in a separate publication.

5 CONCLUSION

An experimental method to measure the temperature amplitude of advected entropy waves in the region of several hundred Hz has been presented. The 2D distribution of line-of-sight integrated temperature agrees well with the qualitative information in the Mie scattering signal of the imaged seeding particles.

The agreement with LES is quite good for lower frequencies. In the higher frequency range further investigations are needed. After the addition of a nozzle, the measured temperature fluctuations will be used to study indirect noise, which is the main motivation of the future work.

REFERENCES

- [1] H. H. Chiu and M. Summerfield. Theory of combustion noise. *Acta Astronautica*, 1(7-8):967–984, 1974.
- [2] A. P. Dowling and Y. Mahmoudi. Combustion noise. *Proceedings of the Combustion Institute*, 35(1):65–100, 2015.
- [3] W. Gardiner, Y. Hidaka, and T. Tanzawa. Refractivity of combustion gases. *Combustion and Flame*, 40:213 – 219, 1981.
- [4] L. Y. Gicquel, N. Gourdain, J.-F. Boussuge, H. Deniau, G. Staffelbach, P. Wolf, and T. Poinsot. High performance parallel computing of flows in complex geometries. *Comptes Rendus Mécanique*, 339(2):104 – 124, 2011. High Performance Computing.
- [5] A. Giusti, N. A. Worth, E. Mastorakos, and A. P. Dowling. Experimental and numerical investigation into the propagation of entropy waves. *AIAA Journal*, 55(2):446–458, 2017.
- [6] F. Marble and S. Candel. Acoustic disturbance from gas non-uniformities convected through a nozzle. *Journal of Sound and Vibration*, 55(2):225 – 243, 1977.
- [7] A. S. Morgans and I. Duran. Entropy noise: A review of theory, progress and challenges. *International Journal of Spray and Combustion Dynamics*, 8(4):285–298, 2016.
- [8] A. S. Morgans, C. S. Goh, and J. A. Dahan. The dissipation and shear dispersion of entropy waves in combustor thermoacoustics. *Journal of Fluid Mechanics*, 733, 2013.
- [9] M. Ota, F. Leopold, R. Noda, and K. Maeno. Improvement in spatial resolution of background-oriented schlieren technique by introducing a telecentric optical system and its application to supersonic flow. *European Transport Research Review*, 7(1):1–10, 2015.
- [10] H. Richard and M. Raffel. Principle and applications of the background oriented schlieren (BOS) method. *Measurement Science and Technology*, 12(9):1576, 2001.
- [11] W. C. Strahle. On combustion generated noise. *Journal of Fluid Mechanics*, 49(2):399–414, 1971.
- [12] L. Venkatakrisnan and G. E. A. Meier. Density measurements using the Background Oriented Schlieren technique. *Experiments in Fluids*, 37(2):237–247, 2004.
- [13] M. Weilenmann, Y. Xiong, M. Bothien, and N. Noiray. Background-oriented schlieren of fuel jet flapping under thermoacoustic oscillations in a sequential combustor. *Journal of Engineering for Gas Turbines and Power*, 141:011030–011030–8, 08 2018.
- [14] Y. Xiong, M. Weilenmann, and N. Noiray. Analysis and Reduction of Spurious Displacements in High-framing-rate Background Oriented Schlieren. *Subm. to Experiments in Fluids*, 2019.